All-optical dual-axis zero-field atomic magnetometer using light-shift modulation

Xiaoyu Li[1,2] Bangcheng Han,[1,2,3,*] Kaixuan Zhang,[2] Ziao Liu,[1,2] Shuying Wang,[1,2,4] Yifan Yan,[1,2,4]
and Jixi Lu[1,2,3,†]

[1]*School of Instrumentation and Optoelectronic Engineering, Beihang University, Beijing 100191, China*
[2]*National Institute of Extremely-Weak Magnetic Field Infrastructure, Hangzhou 310051, China*
[3]*Hefei National Laboratory, Hefei 230088, China*
[4]*Shen Yuan Honors College, Beihang University, Beijing 100191, China*

Functional imaging equipment based on miniaturized atomic magnetometers with array arrangement exhibits promising prospects in biomagnetic scenarios. However, crosstalk from the modulated magnetic field between adjacent sensors degrades the imaging accuracy. To address this issue, this study proposes an all-optical dual-axis zero-field atomic magnetometer using light-shift modulation. We utilize an acousto-optic modulator to modulate a detuned circularly polarized beam for pumping the atomic spin ensembles. This beam allows for the optical modulation of spin polarization and meanwhile generates a light-shift modulation, effectively replacing the conventional magnetic field modulation. By using a probe beam to detect the optical rotation angle perpendicular to the direction of the pump beam, we construct an all-optical configuration of a longitudinally modulated atomic magnetometer, enabling dual-axis magnetic field measurements. Experimental results demonstrate dual-axis sensitivities of 29 and 15 fT/Hz$^{1/2}$, respectively. This method eliminates the need for conventional coil-based magnetic field modulation, thereby paving the way for potential applications in magnetocardiography and magnetoencephalography.

I. INTRODUCTION

Atomic magnetometers have wide-range applications in fundamental physics research [1,2], magnetic anomaly detection [3,4], and biomagnetism [5–7]. The general operating principle is based on optically pumping atomic spin ensembles and detecting Larmor precession in a magnetic field [8]. Zero-field atomic magnetometers (ZFAMs), almost all operating in the spin-exchange relaxation-free (SERF) regime, offer fT or even sub-fT sensitivity [9–11]. Owing to their ultrahigh sensitivity and lack of cryogenic cooling requirements, ZFAMs are poised to serve as a viable alternative to superconducting quantum interference devices (SQUIDs) in biomagnetic scenarios, particularly for magnetocardiography (MCG) [12,13] and magnetoencephalography (MEG) [14,15].

Conventional ZFAMs typically enable single-axis measurement of magnetic fields perpendicular to the pump-probe plane [8]. To achieve multiaxis measurements and acquire more comprehensive magnetic field information, various methods have been proposed [16–19]. The most common approach for multiaxis magnetic field measurement involves the use of high-frequency modulation fields

through magnetic field coils [20–26]. For instance, Li *et al.* proposed a scheme to achieve transverse dual-axis magnetic field measurement by applying a high-frequency modulation field in the direction of the pump light, i.e., *Z*-mode magnetometers [22]. Osborne *et al.* performed transverse dual-axis magnetic field measurements by utilizing a single pump light and applying two separate modulation fields in the transverse direction perpendicular to the pump beam [23]. Building upon this work, they introduced an orthogonal pump beam and a third modulation field to enable triaxial magnetic field measurements [24]. Li *et al.* and Wang *et al.* also achieved triaxial magnetic field measurements by applying high-frequency modulated magnetic fields of different frequencies in different directions [25,26].

Recent research in the field of cardio-brain magnetism has demonstrated that multiaxis magnetic field measurements can provide additional magnetic field information, allowing differentiation between real brain activity and interfering magnetic sources, as well as eliminating artifacts caused by head movement. This ultimately leads to an improved reconstruction of magnetic sources [27]. Currently, multiaxis magnetic field measurements are utilized in array-based magnetometer applications. However, the introduction of high-frequency modulation fields in these applications can lead to crosstalk between adjacent

---
*hanbangcheng@buaa.edu.cn
†lujixi@buaa.edu.cn

sensors, which can significantly affect both the sensor gain and orientation of the sensitive axis of detection [28,29].

Given the prevailing circumstances, an all-optical configuration for ZFAMs represents an optimal approach. Jiménez-Martínez *et al.* proposed a method based on the configuration of transverse magnetic field modulated atomic magnetometers, i.e., X-mode magnetometers. The difference is that a transverse modulated beam is added and utilizes the light-shift modulation magnetic field generated by the beam to replace the original transverse modulated magnetic field. Although this method is all-optical, it adds an extra transverse light field to achieve single-axis measurements with a sensitivity of 2 pT/Hz$^{1/2}$ [30]. Tang *et al.* developed a scheme based on the orthogonal pump-probe configuration operating in dc mode. The difference lies in the substitution of the pump light with an amplitude-modulated pump light aiming to enhance the bandwidth significantly. However, they did not achieve multiaxis magnetic field measurements [31]. Therefore, there is a need for an all-optical multiaxis magnetic field measurement investigation.

In this study, an all-optical dual-axis zero-field atomic magnetometer using light-shift modulation is proposed. We utilize a detuned circularly polarized beam that is modulated by an acousto-optic modulator (AOM) to pump the atomic spin ensembles. This beam ingeniously allows for the optical modulation of spin polarization and meanwhile generates a light-shift modulation replacing the coil-generated modulated magnetic field to constitute an alternative all-optical Z-mode configuration. We demonstrate the feasibility of the method in principle and experiment. Finally, the parameters are optimized to achieve high-sensitivity all-optical dual-axis magnetic field measurements. We anticipate that this method will find application in high-spatial-density array-based magnetometers.

II. PRINCIPLE

The dynamics of the polarized electron spin can be described by the following Bloch equation [32]:

$$\frac{d}{dt}\mathbf{S} = \frac{1}{q}\left[\gamma^e \mathbf{B} \times \mathbf{S} + R_{\text{op}}\left(\frac{1}{2}\mathbf{s} - \mathbf{S}\right) - R_{\text{rel}}\mathbf{S}\right], \quad (1)$$

where q is the slowing-down factor, $\gamma^e = 2\pi \times 28$ Hz/nT is the electron gyromagnetic ratio, $\mathbf{B}$ is the magnetic field vector, $\mathbf{S} = (S_x, S_y, S_z)$ is the electron spin vector, R_{op} is the optical pump rate, $\mathbf{s}$ is the optical pump vector, the propagation direction of the pump light is along the $\hat{z}$ axis, the magnitude of $\mathbf{s}$ is 1 when the pump light is circularly polarized, and R_{rel} is the spin relaxation rate.

If the circularly polarized pump light is detuned, it can induce a light shift along its propagation direction, which results from the ac Stark shift caused by the interaction between the ground-state alkali atoms and the detuned

circularly polarized pump light [33,34]. In the pressure-broadened regime, this light shift can be considered as a fictitious magnetic field, denoted as $\mathbf{B}_{\text{LS}}$ and given by [32]

$$|\mathbf{B}_{\text{LS}}| = \frac{r_e c f_{\text{D1}}}{\gamma^e}\frac{I}{h\upsilon}\frac{\upsilon - \upsilon_{\text{D1}}}{(\upsilon - \upsilon_{\text{D1}})^2 + (\Gamma_{\text{D1}}/2)^2}, \quad (2)$$

where r_e is the classical electron radius, c is the speed of light, f_{D1} is the oscillator strength of the D1 transition of alkali atoms, υ is the pump light frequency, υ_{D1} is the resonance frequency of alkali atoms D1 line, Γ_{D1} is the pressure broadening of alkali atoms D1 line, I is the pump light intensity, and h is Planck's constant.

By employing a detuned circularly polarized light that is sinusoidally modulated with frequency ω_{mod} along the $\hat{z}$ axis to pump the electron spin, we can achieve optical modulation of spin polarization and meanwhile generate a light-shift modulation. Therefore, the modulation is no longer dependent on the modulation fields introduced by conventional magnetic field coils. The time-varying light-shift modulation can be expressed as

$$B_{\text{LS}}(t) = B_{\text{LS}}^0 + B_{\text{LS}}^{\text{mod}}\cos(\omega_{\text{mod}}t), \quad (3)$$

where B_{LS}^0 is a fictitious bias magnetic field and can be compensated to zero. Since the magnetometer configuration is insensitive to the magnetic field in this direction, the incomplete compensation and the drift are not limiting challenge in this magnetometry scheme. $B_{\text{LS}}^{\text{mod}}$ can be deduced by Eq. (2).

The optical modulation of spin polarization can be expressed as

$$R_{\text{op}}(t) = R_{\text{op}}^0 + R_{\text{op}}^{\text{mod}}\cos(\omega_{\text{mod}}t), \quad (4)$$

where R_{op}^0 is the static pump rate. The magnitude of $R_{\text{op}}^{\text{mod}}$ is given by [32]

$$R_{\text{op}}^{\text{mod}} = r_e c f_{\text{D1}}\frac{I}{h\upsilon}\frac{\Gamma_{\text{D1}}/2}{(\upsilon - \upsilon_{\text{D1}})^2 + (\Gamma_{\text{D1}}/2)^2}. \quad (5)$$

When the atomic magnetometer is operating in a near-zero magnetic field, the change of S_z induced by the magnetic field is negligible due to the effect of optical pumping. Therefore, S_z can be regarded as a constant and the transverse dynamics of the polarized electron spin, characterized by $S^* = S_x + iS_y$, can be described by the modified Bloch equation:

$$\frac{d}{dt}S^* = [i\gamma B_{\text{LS}}^{\text{mod}}\cos(\omega_{\text{mod}}t) - \Gamma'(t)]S^* + \gamma(B_0^y - iB_0^x)S_z, \quad (6)$$

where B_0^x and B_0^y are the x-axis and y-axis magnetic fields to be measured, respectively, $\gamma = \gamma^e/q$, and $\Gamma'(t) = [R_{\text{op}}(t) + R_{\text{rel}}]/q$.

The solution of Eq. (6) can be expressed as a general solution:

$$S^*(t) = e^{-\Gamma'_0 t} e^{i\beta \sin(\omega_{\text{mod}} t)} e^{-u \sin(\omega_{\text{mod}} t)}$$
$$\times \left(\int D e^{\Gamma'_0 t} e^{-i\beta \sin(\omega_{\text{mod}} t)} e^{u \sin(\omega_{\text{mod}} t)} dt + C \right), \tag{7}$$

where $\Gamma'_0 = (R^0_{\text{op}} + R_{\text{rel}})/q$, $\beta = \gamma B^{\text{mod}}_{\text{LS}}/\omega_{\text{mod}}$, $u = R^{\text{mod}}_{\text{op}} / (q\omega_{\text{mod}})$, $D = \gamma(B^y_0 - iB^x_0)S_z$, and C is a constant.

Equation (7) is solved to obtain a comprehensive analytical expression by defining β and introducing the Jacobi-Anger expansion and Taylor series expansion as follows:

$$e^{i\beta \sin(\omega_{\text{mod}} t)} = \sum_{n=-\infty}^{\infty} J_n(\beta) e^{in\omega_{\text{mod}} t}, \tag{8}$$

$$e^{-i\beta \sin(\omega_{\text{mod}} t)} = \sum_{m=-\infty}^{\infty} J_m(\beta) e^{-im\omega_{\text{mod}} t}, \tag{9}$$

$$e^{u \sin(\omega_{\text{mod}} t)} = 1 + u \sin(\omega_{\text{mod}} t) + \mathrm{O}(u \sin(\omega_{\text{mod}} t))^2, \tag{10}$$

where $J_n(\beta)$ and $J_m(\beta)$ are the Bessel functions of the first kind of order n and m, respectively. If the modulation frequency ω_{mod} is on the order of kilohertz, $R^{\text{mod}}_{\text{op}} \ll q\omega_{\text{mod}}$, that is, u is significantly small. Therefore, the higher-order terms of the Taylor expansion in Eq. (10) can be neglected, and Eq. (7) can be derived as follows:

$$S^*(t) = \sum_{n=-\infty}^{\infty} \sum_{m=-\infty}^{\infty} J_n(\beta) J_m(\beta) \frac{[\gamma(B^y_0 - iB^x_0)S_z]e^{i(n-m)\omega_{\text{mod}} t}}{\Gamma'_0 - im\omega_{\text{mod}}}$$
$$+ \sum_{n=-\infty}^{\infty} \sum_{m=-\infty}^{\infty} J_n(\beta) J_m(\beta) \frac{[\gamma(B^y_0 - iB^x_0)S_z]e^{i(n-m)\omega_{\text{mod}} t}}{\Gamma'_0 - im\omega_{\text{mod}}}$$
$$[-u \sin(\omega_{\text{mod}} t)]$$
$$+ \sum_{n=-\infty}^{\infty} \sum_{m=-\infty}^{\infty} J_n(\beta) J_m(\beta)[\gamma(B^y_0 - iB^x_0)S_z]e^{-\Gamma'_0 t}$$
$$\times e^{in\omega_{\text{mod}} t} \int u \sin(\omega_{\text{mod}} t) e^{\Gamma'_0 t} e^{-im\omega_{\text{mod}} t} dt$$
$$+ \sum_{n=-\infty}^{\infty} \sum_{m=-\infty}^{\infty} J_n(\beta) J_m(\beta)[\gamma(B^y_0 - iB^x_0)S_z]$$
$$e^{-\Gamma'_0 t} e^{in\omega_{\text{mod}} t}[-u \sin(\omega_{\text{mod}} t)]$$
$$\times \int u \sin(\omega_{\text{mod}} t) e^{\Gamma'_0 t} e^{-im\omega_{\text{mod}} t} dt. \tag{11}$$

Because the third and fourth terms are significantly smaller than the first two terms, they can be neglected. The response $S_x(t) = \mathrm{Re}[S^*(t)]$ for the zero-order parametric resonance ($m = 0$) is observed as follows:

$$S_x(t) = \gamma^e S_z J_0(\beta) \sum_{n=-\infty}^{\infty} J_n(\beta)$$
$$\frac{B^y_0 \cos(n\omega_{\text{mod}} t) + B^x_0 \sin(n\omega_{\text{mod}} t)}{R^0_{\text{op}} + R_{\text{rel}}}$$
$$- \gamma^e S_z J_0(\beta) \sum_{n=-\infty}^{\infty} J_n(\beta)$$
$$\times \frac{B^y_0 \cos(n\omega_{\text{mod}} t) + B^x_0 \sin(n\omega_{\text{mod}} t)}{R^0_{\text{op}} + R_{\text{rel}}} u \sin(\omega_{\text{mod}} t). \tag{12}$$

For the first term, there exists a dc component when $n = 0$, and a first-harmonic component when $n = \pm 1$. The second term has a first-harmonic component when $n = 0$, and both dc and second-harmonic components when $n = \pm 1$.

Therefore, the dc and first-harmonic components of S_x can be expressed as follows:

$$S_{x-\text{dc}}(t) = \gamma^e S_z J^2_0(\beta) \frac{B^y_0}{R^0_{\text{op}} + R_{\text{rel}}} - \gamma^e S_z J_0(\beta) J_1(\beta)$$
$$\frac{B^x_0}{R^0_{\text{op}} + R_{\text{rel}}} u, \tag{13}$$

$$S_{x-\omega_{\text{mod}}}(t) = 2\gamma^e S_z J_0(\beta) J_1(\beta) \frac{B^x_0}{R^0_{\text{op}} + R_{\text{rel}}} \sin(\omega_{\text{mod}} t)$$
$$- \gamma^e S_z J^2_0(\beta) \frac{B^y_0}{R^0_{\text{op}} + R_{\text{rel}}} u \sin(\omega_{\text{mod}} t). \tag{14}$$

As mentioned earlier, $u \ll 1$. This results in the fact that the second terms in Eqs. (13) and (14) are significantly smaller compared to the first term, indicating that $S_{x-\text{dc}}$ and $S_{x-\omega_{\text{mod}}}$ are primarily sensitive to B^y_0 and B^x_0, respectively. Therefore, transverse dual-axis magnetic field measurements can be performed by demodulating the dc and first-harmonic components.

However, Eqs. (13) and (14) indicate that $S_{x-\text{dc}}$ and $S_{x-\omega_{\text{mod}}}$ also contain nonsensitive-axis crosstalk. The reason for this is because the optical pump rate is also modulated, that is $R^{\text{mod}}_{\text{op}} \cos(\omega_{\text{mod}} t)$. It leads to the $u \sin(\omega_{\text{mod}} t)$ presence in Eq. (10). Therefore, within this system, the nonsensitive-axis crosstalk is inherently caused by fundamental experimental principles of optical modulation and can only be minimized through parameter optimization rather than being completely eliminated. In the dc demodulation mode, the y axis is considered as the measurement sensitive axis, while x axis is regarded as nonsensitive axis; thus the nonsensitive-axis crosstalk is expressed as C^{dc}_{xy}. In contrast, for the first-harmonic demodulation mode, x axis serves as a measurement sensitive axis and y axis acts as a
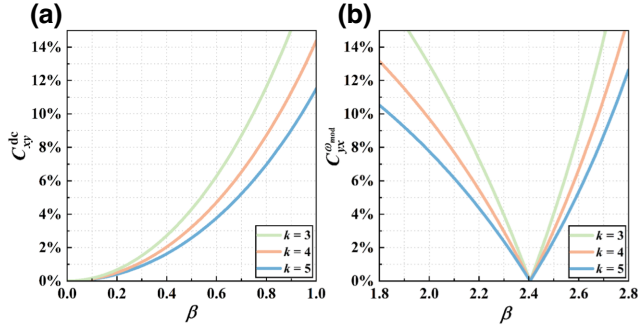
FIG. 1. Simulation results of the nonsensitive-axis crosstalk according to Eqs. (17) and (18) in (a) dc demodulation and (b) first-harmonic demodulation.

nonsensitive axis; hence the nonsensitive-axis crosstalk is expressed as $C_{yx}^{\omega\,\text{mod}}$ accordingly.

$$C_{xy}^{\text{dc}} = \frac{\gamma^e S_z J_0(\beta) J_1(\beta)(1/(R_{\text{op}}^0 + R_{\text{rel}}))u}{\gamma^e S_z J_0^2(\beta)(1/(R_{\text{op}}^0 + R_{\text{rel}}))} = \frac{J_1(\beta)}{J_0(\beta)}u,$$
(15)

$$C_{yx}^{\omega\,\text{mod}} = \frac{\gamma^e S_z J_0^2(\beta)(1/(R_{\text{op}}^0 + R_{\text{rel}}))u}{2\gamma^e S_z J_0(\beta) J_1(\beta)(1/(R_{\text{op}}^0 + R_{\text{rel}}))} = \frac{J_0(\beta)}{2J_1(\beta)}u.$$
(16)

To decouple the parameters β and u and simultaneously minimize the nonsensitive-axis crosstalk, we define the detuning factor $k = (\upsilon - \upsilon_{\text{D1}})/(\Gamma_{\text{D1}}/2)$, and thus, $u = \beta/k$. Therefore, Eqs. (15) and (16) can be further expressed as follows:

$$C_{xy}^{\text{dc}} = \frac{J_1(\beta)}{J_0(\beta)} \frac{\beta}{k},$$
(17)

$$C_{yx}^{\omega\,\text{mod}} = \frac{J_0(\beta)}{2J_1(\beta)} \frac{\beta}{k}.$$
(18)

From the simulation results as shown in Figs. 1(a) and 1(b), it is evident that as the value of k increases, the nonsensitive-axis crosstalk decreases. By optimizing the parameter β, the nonsensitive-axis crosstalk can be minimized. The parameters k and β are related to the frequency detuning and intensity of the pump light. Therefore, the nonsensitive-axis crosstalk can be minimized by optimizing the frequency detuning and intensity of the pump light in experiments.

III. EXPERIMENTAL SETUP AND PROCEDURE

The experimental setup is depicted in Fig. 2. A cubic Pyrex glass cell with an internal dimension of 8 mm is
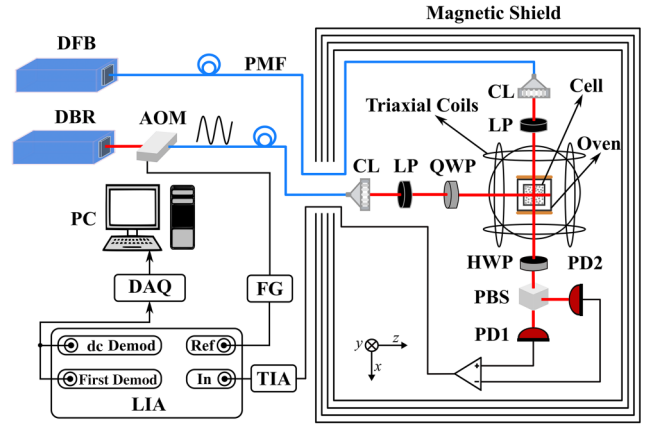

FIG. 2. Schematic of the experimental setup. DFB, distributed feedback laser; DBR, distributed Bragg reflector laser; AOM, acousto-optic modulator; PMF, polarization-maintaining fiber; CL, collimator; LP, linear polarizer; QWP, quarter-wave plate; HWP, half-wave plate; PBS, polarization beam splitter; PD, photodiode; TIA, transimpedance amplifier; LIA, lock-in amplifier; FG, function generator; DAQ, data acquisition.

the core sensing element. It contains a droplet of isotopically enriched [87]Rb metal, about 2100 Torr [4]He buffer gas, and 70 Torr N2 quenching gas, with the spin-destruction collision relaxation rate of 256 s^{-1} and the wall-collision relaxation rate of 23 s^{-1}. Its pressure broadening is about 61.5 GHz. The cell is placed within a boron-nitride oven, and the wall of the oven has two flexible heating films attached to it. These heating films are powered by high-frequency ac currents at 500 kHz, raising the temperature to 160 °C. The four-layer μ-metal cylindrical magnetic shield barrel is used to attenuate the geomagnetic field down to about 3 nT. Additionally, a set of triaxial coils compensate for the residual magnetic field and generate the calibration field [35].

A distributed Bragg reflector (DBR) laser is used to generate approximately 10 mW of pump light incident to the cell, which has a spot diameter of 1.4 mm. The pump beam is detuned by roughly 150 GHz from the center of the [87]Rb D1 line. To modulate the amplitude of the pump beam, an AOM is employed and driven by a sinusoidal signal. The resultant fictitious magnetic field $B_{\text{LS}}^{\text{mod}}$ varies within the range of 3–260 nT and the $R_{\text{op}}^{\text{mod}}$ varies within the range of 91–9100 s^{-1}. The pump beam is then transmitted to the magnetometer through a polarization-maintaining fiber (PMF) with an extinction ratio adjusted to exceed 20 dB. The circular polarization is achieved by passing the linearly polarized pump beam through a linear polarizer and a quarter-wave plate. This detuned circularly polarized pump beam modulates the spin polarization and meanwhile generates light-shift modulation [36,37]. Additionally, a distributed feedback (DFB) laser is used to generate about 4 mW of probe light incident to the cell, which
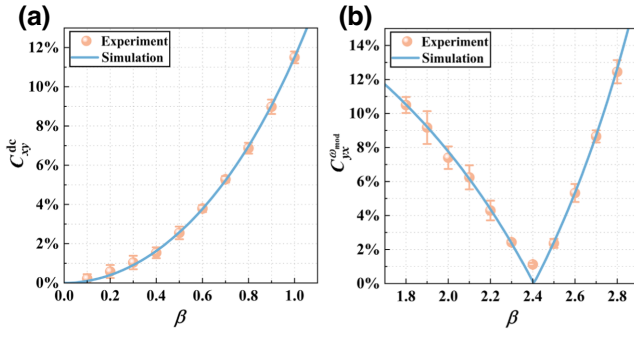
(a)

(b)

FIG. 3. Comparison of the simulated and experimental nonsensitive-axis crosstalk in (a) dc demodulation and (b) first-harmonic demodulation for $k = 5$. The blue curves represent simulated nonsensitive-axis crosstalk, and the orange error bars depict experimentally measured nonsensitive-axis crosstalk.

is transmitted to the magnetometer through a PMF. The probe beam is detuned by roughly 130 GHz from the center of the ^{87}Rb D1 line. The beam passes through a linear polarizer. The balanced polarization differential detection is utilized to detect the rotation angle of the transmitted probe beam. The current signal from the photodetectors (Hamamatsu, S10355-01) is converted to a voltage signal by a transimpedance amplifier (Thorlabs, PDA200C). This voltage signal is then input into a lock-in amplifier (Zurich Instruments, MFLI) for dc and first-harmonic demodulation. The modulation frequency of 1 kHz, generated by a function generator (Keysight, 33522B), controls the AOM and serves as the reference input for demodulation. The demodulation signals from the magnetometer are acquired and recorded using a data-acquisition system (NI, PXIe-4464).

During the experiment, we configured the device to operate in optical modulation mode, following the previously described experimental setup. Subsequently, we minimized the nonsensitive-axis crosstalk by adjusting the frequency detuning and intensity of the pump light. To measure the nonsensitive-axis crosstalk, we applied a calibration magnetic field to both axes, respectively, recorded the magnetometer response from each axis, and subsequently divided the responses to obtain the nonsensitive-axis crosstalk [38,39]. Finally, we evaluated the sensitivity of the magnetometer by separately measuring the amplitude frequency response and noise floor of each axis. The sensitivity was calculated by dividing the noise spectrum by the respective amplitude frequency response.

IV. EXPERIMENTAL RESULTS AND DISCUSSIONS

A. Optimization of the nonsensitive-axis crosstalk

The nonsensitive-axis crosstalk can lead to degradation of the measurement accuracy. From the simulation results

as shown in Figs. 1(a) and 1(b), it is evident that when β is fixed at a certain value, increasing the value of k leads to a decrease in the nonsensitive-axis crosstalk. Therefore, the frequency of the pump light should be far detuned from the resonance frequency of ^{87}Rb D1 line to minimize the nonsensitive-axis crosstalk. This will also result in a larger power of the pump light required for experiments. Due to experimental conditions, the frequency detuning in experiments was roughly 150 GHz, corresponding to $k = 5$. Under this condition, we adjusted the power of the pump light. When the pump light incident to the cell was approximately 0.5 and 12.5 mW, corresponding to $\beta = 0.1$ and $\beta = 2.4$, the nonsensitive-axis crosstalk C_{xy}^{dc} and $C_{yx}^{\omega\,mod}$ were minimized, respectively. At these operational points, the simulation results of the nonsensitive-axis crosstalk were 0.1% and near zero as shown in Figs. 3(a) and 3(b), whereas the experimental results were 0.21% and 1.12%. A reasonable explanation for the difference between the experimental and simulation results was the existence of the nonorthogonality between the lights and magnetic fields. This can be solved by improving the machining and assembly accuracy of the device.

Another issue is how to further reduce the nonsensitive axis crosstalk. It can be seen from Eqs. (17) and (18) that the value of k needs to be increased, which leads to greater detuning and a decrease in pump rate. Therefore, it is necessary to correspondingly increase the light intensity when detuning is increased. However, due to the lasers used in the actual experiments, the detuning range and light power are limited, with a maximum detuning frequency of
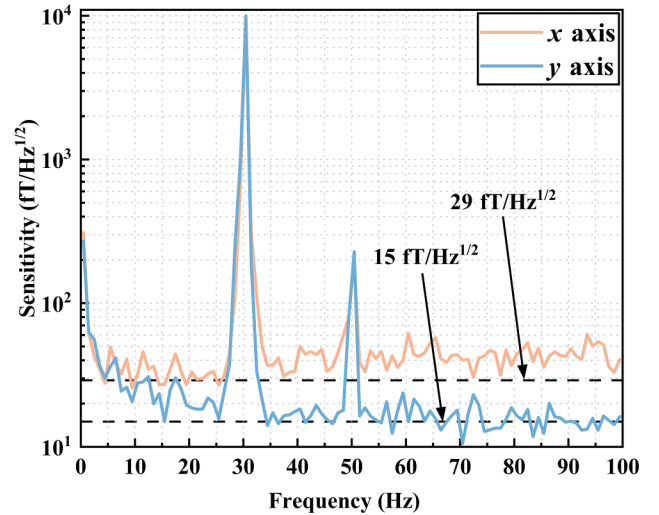

FIG. 4. Sensitivities of the all-optical dual-axis zero-field atomic magnetometer. The results include a calibration magnetic field with a frequency of 30.5 Hz, an amplitude of 10 pTrms, and an additional peak at 50 Hz introduced by industrial frequency interference.
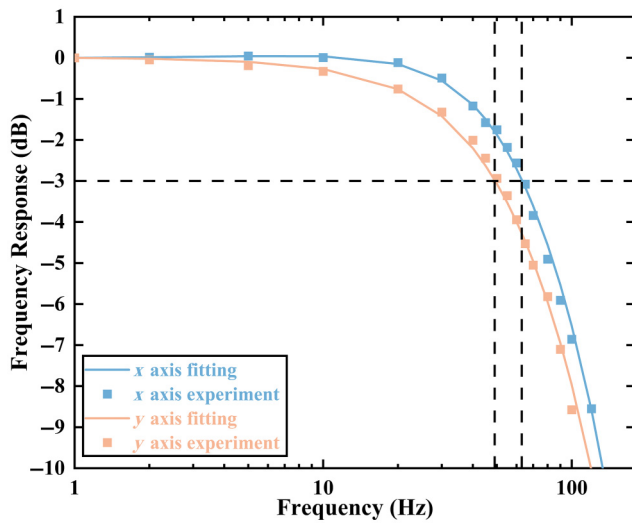
FIG. 5. Frequency response of the all-optical dual-axis zero-field atomic magnetometer. The solid lines (solid boxes) represent the results obtained from fitting (experimental) data.

150 GHz and a maximum light power of 15 mW entering the magnetometer after fiber coupling. For instance, if the laser is selected to meet the requirements of increasing the detuning amount to 200 GHz and the light power to 30 mW, the nonsensitive axis crosstalk can continue to be suppressed to less than 1%.

B. Sensitivity and bandwidth

The magnetometer sensitivities were measured to be 29 and 15 fT/Hz$^{1/2}$ as shown in Fig. 4. Owing to the difference in scale factors between the x and y axes, the sensitivity along the y axis is superior to that along the x axis. The sensitivities can be further improved through optimization of the intensity and frequency detuning. However, this would result in increased nonsensitive-axis crosstalk, meaning that the all-optical magnetometer cannot accurately measure magnetic fields along both sensitive axes. Therefore, we measured sensitivities in overall consideration of nonsensitive-axis crosstalk and the obtained sensitivities remained sufficiently high.

The bandwidth is also a crucial metric for characterizing the performance of a magnetometer. It is defined as the frequency range within which the response amplitude exceeds −3 dB. We conducted measurements on the frequency response of the all-optical dual-axis zero-field atomic magnetometer and obtained an x-axis bandwidth of 63 Hz and a y-axis bandwidth of 49 Hz (Fig. 5).

V. CONCLUSIONS

We developed an all-optical dual-axis zero-field atomic magnetometer using light-shift modulation. By employing a detuned circularly polarized beam that is sinusoidally modulated by an AOM, we achieved optical modulation of the spin polarization and generated light-shift modulation. This approach eliminates the need for conventional coil-based magnetic field modulation, which can introduce crosstalk between adjacent sensors in array-based applications. The method was validated experimentally, demonstrating a sensitivity of 29 fT/Hz$^{1/2}$ on the x axis and 15 fT/Hz$^{1/2}$ on the y axis. In the future, the method proposed in this study can be further applied to an integrated VCSEL atomic magnetometer, allowing light-shift modulation through laser current modulation. This advancement will make the magnetometer more suitable for high-spatial-density array-based applications, such as MCG and MEG.

[1] M. Jiang, Y. Qin, X. Wang, Y. Wang, H. Su, X. Peng, and D. Budker, Floquet spin amplification, Phys. Rev. Lett. **128,** 233201 (2022).

[2] Y. Wang, Y. Huang, C. Guo, M. Jiang, X. Kang, H. Su, Y. Qin, W. Ji, D. Hu, X. Peng, and D. Budker, Search for exotic parity-violation interactions with quantum spin amplifiers, Sci. Adv. **9,** eade0353 (2023).

[3] X. Bi, L. Ruan, Z. Liu, K. Li, Y. Ruan, W. Zheng, and Q. Lin, Quantitative analysis of magnetic cobalt particles with an optically pumped atomic magnetometer, Appl. Phys. Lett. **118,** 084101 (2021).

[4] H. Yao, B. Maddox, and F. Renzoni, High-sensitivity operation of an unshielded single cell radio-frequency atomic magnetometer, Opt. Express **30,** 42015 (2022).

[5] X. Ru, K. He, B. Lyu, D. Li, W. Xu, W. Gu, X. Ma, J. Liu, C. Li, T. Li, F. Zheng, X. Yan, X. Yin, H. Duan, S. Na, S. Wan, J. Qin, J. Sheng, and J.-H. Gao, Multimodal neuroimaging with optically pumped magnetometers: A simultaneous MEG-EEG-FNIRS acquisition system, NeuroImage **259,** 119420 (2022).

[6] Y. Ruan, X. He, L. Ruan, F. Liu, Z. Zhang, J. Weng, Q. Yan, G. Zhang, K. Li, W. Zheng, and Q. Lin, Drug monitoring by optically pumped atomic magnetometer, IEEE Photonics J. **14,** 3134305 (2022).

[7] K. K. G. Kurian, S. S. Sahoo, P. K. Madhu, and G. Rajalakshmi, Single-beam room-temperature atomic magnetometer with large bandwidth and dynamic range, Phys. Rev. Appl. **19,** 054040 (2023).

[8] J. C. Allred, R. N. Lyman, T. W. Kornack, and M. V. Romalis, High-sensitivity atomic magnetometer unaffected by spin-exchange relaxation, Phys. Rev. Lett. **89,** 130801 (2002).

[9] I. K. Kominis, T. W. Kornack, J. C. Allred, and M. V. Romalis, A subfemtotesla multichannel atomic magnetometer, Nature **422**, 596 (2003).

[10] M. P. Ledbetter, I. M. Savukov, V. M. Acosta, D. Budker, and M. V. Romalis, Spin-exchange-relaxation-free magnetometry with Cs vapor, Phys. Rev. A **77**, 033408 (2008).

[11] D. Sheng, S. Li, N. Dural, and M. V. Romalis, Subfemtotesla scalar atomic magnetometry using multipass cells, Phys. Rev. Lett. **110**, 160802 (2013).

[12] Y. J. Kim, I. Savukov, and S. Newman, Magnetocardiography with a 16-channel fiber-coupled single-cell Rb optically pumped magnetometer, Appl. Phys. Lett. **114**, 143702 (2019).

[13] W. Xiao, C. Sun, L. Shen, Y. Feng, M. Liu, Y. Wu, X. Liu, T. Wu, X. Peng, and H. Guo, A movable unshielded magnetocardiography system, Sci. Adv. **9**, eadg1746 (2023).

[14] M. Rea, E. Boto, N. Holmes, R. Hill, J. Osborne, N. Rhodes, J. Leggett, L. Rier, R. Bowtell, V. Shah, and M. J. Brookes, A 90-channel triaxial magnetoencephalography system using optically pumped magnetometers, Ann. N. Y. Acad. Sci. **1517**, 107 (2022).

[15] Y. Chen, L. Zhao, Y. Ma, M. Yu, Y. Wang, N. Zhang, K. Wei, and Z. Jiang, Spin exchange optically pumped nuclear spin self compensation system for moving magnetoencephalography measurement, Biomed. Opt. Express **13**, 5937 (2022).

[16] E. Zhivun, M. Bulatowicz, A. Hryciuk, and T. Walker, Dual-axis π-pulse magnetometer with suppressed spin-exchange relaxation, Phys. Rev. Appl. **11**, 034040 (2019).

[17] H. F. Dong, J. C. Fang, B. Q. Zhou, X. B. Tang, and J. Qin, Three-dimensional atomic magnetometry, Eur. Phys. J. Appl. Phys. **57**, 21004 (2012).

[18] F. Lu, J. Lu, B. Li, Y. Yan, S. Zhang, K. Yin, M. Ye, and B. Han, Triaxial vector operation in near-zero field of atomic magnetometer with femtotesla sensitivity, IEEE Trans. Instrum. Meas. **71**, 1501210 (2022).

[19] M. V. Petrenko, A. S. Pazgalev, and A. K. Vershovskii, All-optical nonzero-field vector magnetic sensor for magnetoencephalography, Phys. Rev. Appl. **20**, 024001 (2023).

[20] Y. Yan, J. Lu, S. Zhang, F. Lu, K. Yin, K. Wang, B. Zhou, and G. Liu, Three-axis closed-loop optically pumped magnetometer operated in the SERF regime, Opt. Express **30**, 18300 (2022).

[21] S. J. Seltzer and M. V. Romalis, Unshielded three-axis vector operation of a spin-exchange-relaxation-free atomic magnetometer, Appl. Phys. Lett. **85**, 4804 (2004).

[22] Z. Li, R. T. Wakai, and T. G. Walker, Parametric modulation of an atomic magnetometer, Appl. Phys. Lett. **89**, 134105 (2006).

[23] V. Shah, J. Osborne, J. Orton, and O. Alem, in *Steep Dispersion Engineering and Opto-Atomic Precision Metrology XI* (2018), Vol. 10548, pp. 89–95.

[24] E. Boto, V. Shah, R. M. Hill, N. Rhodes, J. Osborne, C. Doyle, N. Holmes, M. Rea, J. Leggett, R. Bowtell, and M. J. Brookes, Triaxial detection of the neuromagnetic field using optically-pumped magnetometry: Feasibility and application in children, NeuroImage **252**, 119027 (2022).

[25] L. Li, J. Tang, B. Zhao, L. Cao, B. Zhou, and Y. Zhai, Single-beam triaxial spin-exchange relaxation-free atomic magnetometer utilizing transverse modulation fields, J. Phys. D: Appl. Phys. **55**, 505001 (2022).

[26] K. Wang, K. Zhang, B. Zhou, F. Lu, S. Zhang, Y. Yan, W. Wang, and J. Lu, Triaxial closed-loop measurement based on a single-beam zero-field optically pumped magnetometer, Front. Phys. **10**, 1059487 (2022).

[27] M. J. Brookes, E. Boto, M. Rea, V. Shah, J. Osborne, N. Holmes, R. M. Hill, J. Leggett, N. Rhodes, and R. Bowtell, Theoretical advantages of a triaxial optically pumped magnetometer magnetoencephalography system, NeuroImage **236**, 118025 (2021).

[28] E. Boto, S. S. Meyer, V. Shah, O. Alem, S. Knappe, P. Kruger, T. M. Fromhold, M. Lim, P. M. Glover, P. G. Morris, R. Bowtell, G. R. Barnes, and M. J. Brookes, A new generation of magnetoencephalography: Room temperature measurements using optically-pumped magnetometers, NeuroImage **149**, 404 (2017).

[29] K.-M. C. Fu, G. Z. Iwata, A. Wickenbrock, and D. Budker, Sensitive magnetometry in challenging environments, AVS Quantum Sci. **2**, 044702 (2020).

[30] R. Jiménez-Martínez, S. Knappe, and J. Kitching, An optically modulated zero-field atomic magnetometer with suppressed spin-exchange broadening, Rev. Sci. Instrum. **85**, 045124 (2014).

[31] J. Tang, Y. Liu, Y. Wang, B. Zhou, B. Han, Y. Zhai, and G. Liu, Enhancement of bandwidth in spin-exchange relaxation-free (SERF) magnetometers with amplitude-modulated light, Appl. Phys. Lett. **120**, 084001 (2022).

[32] S. J. Seltzer, *Developments in Alkali-Metal Atomic Magnetometry* (Princeton University, Princeton, 2008), pp. 11–57.

[33] W. Happer and B. S. Mathur, Effective operator formalism in optical pumping, Phys. Rev. **163**, 12 (1967).

[34] C. Cohen-Tannoudji and J. Dupont-Roc, Experimental study of Zeeman light shifts in weak magnetic fields, Phys. Rev. A **5**, 968 (1972).

[35] J. Lu, S. Wang, F. Lu, C. Lu, X. Zhang, and D. Ma, Hybrid optimal design of square highly uniform magnetic field coils, IEEE Trans. Ind. Electron. **70**, 4236 (2023).

[36] B. Patton, E. Zhivun, D. C. Hovde, and D. Budker, All-optical vector atomic magnetometer, Phys. Rev. Lett. **113**, 013001 (2014).

[37] E. Zhivun, A. Wickenbrock, B. Patton, and D. Budker, Alkali-vapor magnetic resonance driven by fictitious radiofrequency fields, Appl. Phys. Lett. **105**, 192406 (2014).

[38] S. Pradhan and R. Behera, Characterization of polarimetric based three axis atomic magnetometer, Sens. Actuators, A **290**, 48 (2019).

[39] Y. Li, M. Ma, Y. Luo, Y. Xie, J. Wang, and F. Xu, in *2021 International Conference of Optical Imaging and Measurement (ICOIM)*, IEEE (2021), pp. 234–238.